

Article

Performance Characteristics of an Orthopter-Type Vertical Axis Wind Turbine in Shear Flows

Rudi Purwo Wijayanto ^{1,2,*}, Takaaki Kono ^{3,*} and Takahiro Kiwata ³¹ Graduate School of Natural Science and Technology, Kanazawa University, Kanazawa 920-1192, Japan² The Agency of the Assessment and Application of Technology (BPPT), Jakarta 10340, Indonesia³ Institute of Science and Engineering, Kanazawa University, Kanazawa 920-1192, Japan; kiwata@se.kanazawa-u.ac.jp

* Correspondence: rudi.purwo@stu.kanazawa-u.ac.jp (R.P.W.); t-kono@se.kanazawa-u.ac.jp (T.K.)

Received: 9 January 2020; Accepted: 2 March 2020; Published: 4 March 2020



Abstract: To properly conduct a micro-siting of an orthopter-type vertical axis wind turbine (O-VAWT) in the built environment, this study investigated the effects of horizontal shear flow on the power performance characteristics of an O-VAWT by performing wind tunnel experiments and computational fluid dynamics (CFD) simulations. A uniform flow and two types of shear flow (advancing side faster shear flow (ASF-SF) and retreating side faster shear flow (RSF-SF)) were employed as the approaching flow to the O-VAWT. The ASF-SF had a higher velocity on the advancing side of the rotor. The RSF-SF had a higher velocity on the retreating side of the rotor. For each type of shear flow, three shear strengths ($\Gamma = 0.28, 0.40$ and 0.51) were set. In the ASF-SF cases, the power coefficients (C_p) were significantly higher than the uniform flow case at all tip speed ratios (λ) and increased with Γ . In the RSF-SF cases, C_p increased with Γ . However, when $\Gamma = 0.28$, the C_p was lower than the uniform flow case at all λ . When $\Gamma = 0.51$, the C_p was higher than the uniform flow case except at low λ ; however, it was lower than the ASF-SF case with $\Gamma = 0.28$. The causes of the features of C_p were discussed through the analysis of the variation of blade torque coefficient, its rotor-revolution component and its blade-rotation component with azimuthal angle by using the CFD results for flow fields (i.e., horizontal velocity vectors, pressure and vorticity). These results indicate that a location where ASF-SFs with high Γ values dominantly occur is ideal for installing the O-VAWT.

Keywords: orthopter; vertical axis wind turbine; power coefficient; torque coefficient; shear flow; wind tunnel; CFD; delayed detached-eddy simulation

1. Introduction

Since the 2000s, interest in installing small wind turbines (SWTs) in the built environment has been growing [1–9]. Wind conditions in the built environment are complex in nature and are characterized by lower wind speeds and higher turbulence because of the presence of obstructions [8,9]. For SWTs to be able to make up their costs within their lifetimes, they should have high efficiency and be placed at sites with high wind speeds, such as coastal sites or high-elevation inland sites. However, in the built environment, keeping the rotational speed of an SWT's rotor as low as possible is preferable from the viewpoint of aerodynamic noise [10,11]. Therefore, the optimal tip-speed ratio of an SWT in the built environment should be as low as possible, while the maximum power coefficient of the SWT should be as high as possible.

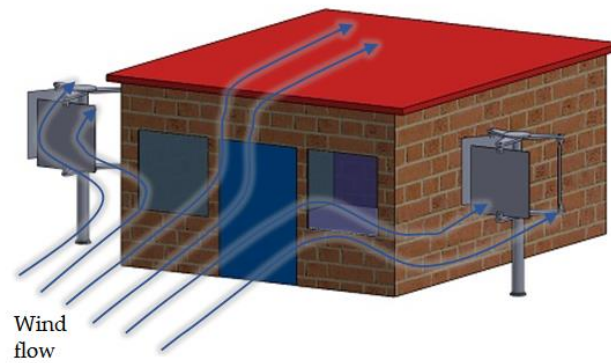
Wind turbines are classified into horizontal-axis wind turbines (HAWTs) and vertical-axis wind turbines (VAWTs), based on the orientation of their rotation axes. Generally, in the built environment, VAWTs are preferable to HAWTs because VAWTs do not suffer, as much as HAWTs, from reduced energy outputs from frequent wind direction changes [12]. Wind turbines are further classified into

lift-type wind turbines and drag-type wind turbines, based on the aerodynamic force component that acts on a blade and dominantly contributes to the rotor rotation. With regard to lift-type VAWTs, a lot of research on Darrieus-type VAWTs, including straight-bladed and helical-bladed ones, has been conducted [13–16]. With regard to drag-type VAWTs, a lot of research on Savonius-type VAWTs has been conducted [17–21]. In general, the optimal tip-speed ratio of a drag-type VAWT is less than 1.0 [11], which is much smaller than that of a lift-type VAWT. Moreover, although the maximum power coefficient of a drag-type VAWT is generally much smaller than that of a lift-type VAWT, the power coefficient of a drag-type VAWT is generally greater than that of a lift-type VAWT at a low tip-speed ratio, of less than 1.0. Therefore, a drag-type VAWT is favorable in the built environment and was researched by our research group.

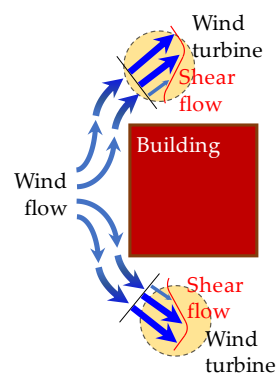
Our group [22,23] researched a drag-type VAWT called the orthopter-type VAWT (O-VAWT). The O-VAWT is a variable-pitch VAWT; each of the flat-plate blades not only revolves around the main shaft but also rotates around its own blade axis, which is rotationally supported by a pair of connecting arms. We investigated the effects of the number and aspect ratio of the flat-plate blades on the power performance of the O-VAWT in a uniform flow by conducting wind tunnel experiments with an open test section and three-dimensional computational fluid dynamics (CFD) simulations. When the number of the blades was three and the aspect ratio of the blades was 1:1, the maximum power coefficient was 0.25 and the optimal tip-speed ratio was 0.4 [22]. Here, the optimal tip-speed ratios of Savonius-type VAWTs are in the range of 0.45 to 1.0 [21]. Except for several studies that were conducted using a wind tunnel with a very high blocking ratio of the closed test section, the maximum power coefficient of the Savonius-type VAWT was, at most, 0.25 [21]. That is, the O-VAWT has a lower optimal tip-speed ratio than Savonius-type VAWTs, although the maximum power coefficient is relatively high. Therefore, from the viewpoint of aerodynamic noise, the O-VAWT can be more favorable in the built environment as compared to Savonius-type VAWTs. Except for our studies, studies on the power performance of O-VAWTs are very limited. Shimizu et al. [24] investigated the effects of the aspect ratio of the blade on the power performance of an O-VAWT with two blades whose cross-sectional shape was an ellipse by conducting wind tunnel experiments. Bayeul-Line et al. [25] examined the effects of the blade's cross-sectional shape (elliptical and straight) and the initial blade stagger angle on the performance of an O-VAWT by conducting 2-dimensional CFD simulations. Cooper and Kennedy [26] examined the power performance of an O-VAWT with three blades whose cross-sectional shape was the upstream half of a NACA0010-65 section reflected about the mid-chord by conducting theoretical analysis with a multiple-stream tube model and field measurements. Our group [23] conducted wind tunnel experiments to compare the performance of an O-VAWT with elliptic blades and one with flat-plate blades. By considering the mechanical loss torque, we obtained the maximum power coefficient of 0.246 at a tip-speed ratio of 0.4 for the O-VAWT with elliptic blades and of 0.288 at a tip-speed ratio of 0.4 for the O-VAWT with flat-plate blades. It should be noted that these studies on O-VAWTs were conducted in conditions where the approaching flows had uniform distribution.

To properly conduct a micro-sitting of an O-VAWT in the built environment, it is important to understand the effects of the strong shear approach flow with on the performance of the O-VAWT. Figure 1 illustrates the approaching wind flow to a building. As the wind flow approaches the building, the wind speed decreases, and the pressure increases. Then, the wind flow proceeds along the upwind face of the building and separates at the corners on the roof and the side walls. As the separated wind flow is not obstructed by the building, the pressure decreases, and the wind speed increases. Near the upwind corners, the wind speed increases more than that of the approaching wind. In addition, reverse flow regions are formed between the separated shear layer and the building's walls. As a result, strong shear flows are formed vertically over the roof surface and horizontally over the side walls. Due to the mixing of momentum, the shear becomes weaker as the flow proceeds downstream. To utilize the increased wind speed over the roof of a building, the effects of building shapes and wind directions on the wind conditions have been investigated (e.g., [27]). Furthermore, the effects of wind conditions, such as wind speed, turbulent intensity, and skew angles, on the potential energy

yield and the power performance of a wind turbine have been studied (e.g., [28,29]). In this study, we investigated the effects of horizontal shear flow on the performance of the O-VAWT by conducting wind tunnel experiments and three-dimensional CFD simulations. A uniform flow and two types of shear flow were employed as the approaching flow to the O-VAWT. One type had a higher velocity on the advancing side of the rotor. The other type had a higher velocity on the retreating side of the rotor. For each type of shear flow, we set three different shear strengths.



(a)



(b)

Figure 1. Illustration of the approaching wind flow to the wind turbine near upwind corners of a building. (a) Bird view; (b) enlarged top view.

2. Experimental Approach

2.1. Wind Turbine Model

In this paper, we employed a right-handed Cartesian coordinate system $(x_1, x_2, x_3) = (x, y, z)$, in which the z -direction was aligned in the vertical direction. The wind turbine used in this study was an O-VAWT with three flat-plate blades as shown in Figure 2. The blade had a height of $h = 4.00 \times 10^{-1}$ m, chord length of $c = 4.00 \times 10^{-1}$ m and thickness of 4.0×10^{-3} m. Each of the blades not only revolved around the main shaft but also rotated around its own blade axis, which was rotationally supported by a pair of connecting arms. The distance between the main shaft and one of the blade axes was $R = 2.55 \times 10^{-1}$ m. In addition, each of the blade axes was connected with the main shaft by a chain via sprockets. Since the ratio of the number of teeth on the sprocket of the main shaft to that of the blade axis was 1:2, each of the blades rotated around the own blade axis a half time while the rotor revolved around the main shaft one time. When seen from the top, the rotor revolved around the main shaft counterclockwise and each of the blades rotated around the own blade axis clockwise as shown in Figure 2c. Therefore, by using the angular velocity of the rotor revolution (ω), the angular

velocity of the blade rotation is expressed as $-\omega/2$. Furthermore, as shown in Figure 2c, according to the azimuthal angle of a blade (φ), we call the range of $90^\circ < \varphi < 270^\circ$ the “upwind region” of the rotor, $0^\circ < \varphi < 90^\circ$ and $270^\circ < \varphi < 360^\circ$ the “downwind region” of the rotor, $180^\circ < \varphi < 360^\circ$ the “advancing side of the rotor” and $0^\circ < \varphi < 180^\circ$ the “retreating side” of the rotor. The O-VAWT is designed so that the drag force on a blade is large on the advancing side of the rotor while being small on the retreating side of the rotor.

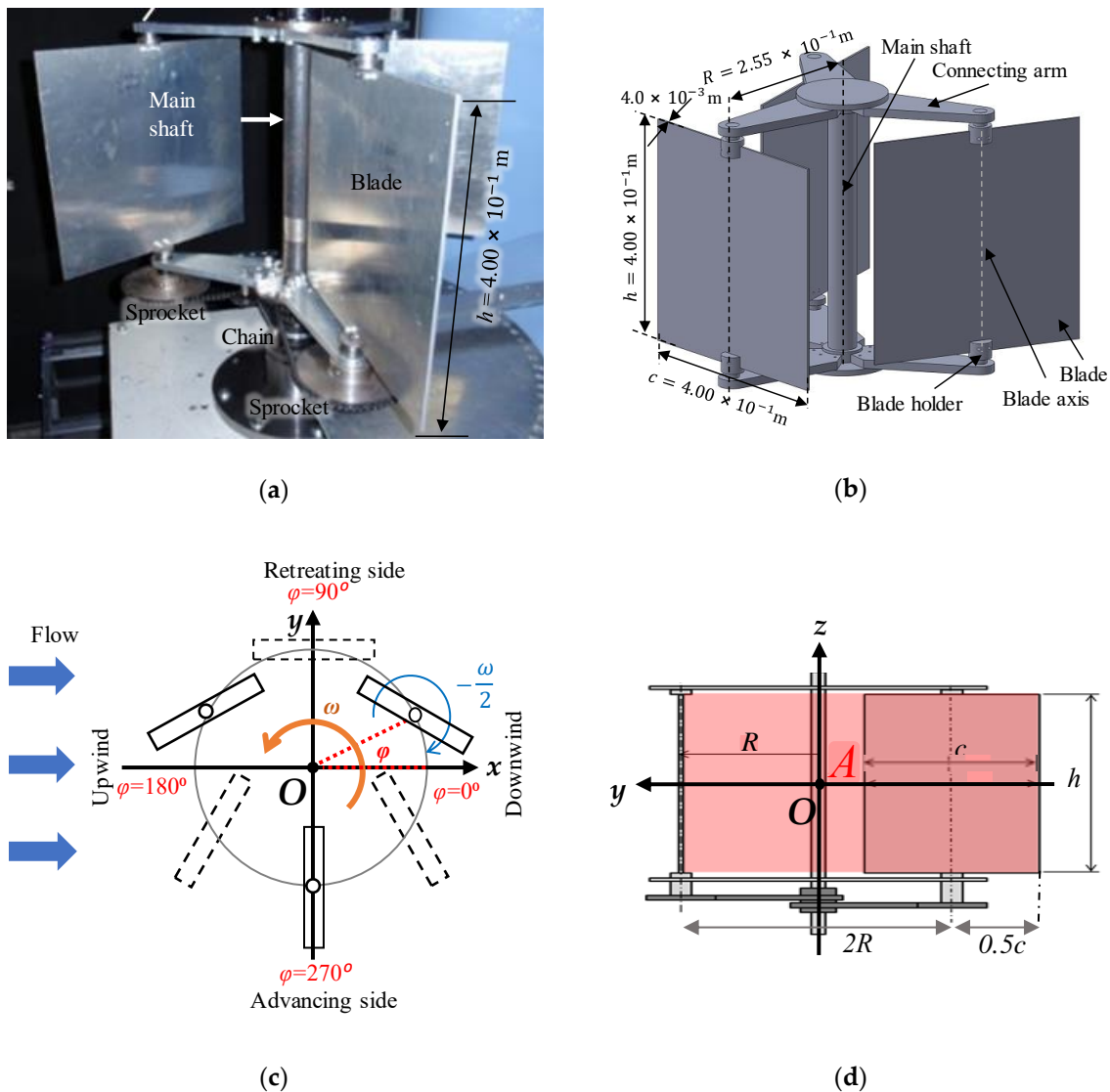


Figure 2. Orthopter-type vertical-axis wind turbine (O-VAWT). (a) A photograph of O-VAWT with three flat blades, main shaft, arm, the chains and sprockets; (b) an isometric view of O-VAWT with three flat blades; (c) motion of rotor and blades viewed from the top; (d) a projected swept area of the rotor viewed from the upwind side.

Figure 2d shows a projected swept area of the rotor (A), which is defined as:

$$A = (2R + 0.5c)h. \tag{1}$$

We define the diameter of the rotor as:

$$D = 2R. \tag{2}$$

The O-VAWT had a rotor's diameter of $D = 5.1 \times 10^{-1}$ m and a projected rotor's swept area of $A = 2.84 \times 10^{-1}$ m² can be considered as a micro wind turbine. A small scale wind turbine that has a diameter up to 1.25 m and the swept area up to 1.2 m² is categorized as a micro wind turbine [4].

2.2. Experimental Setup for Uniform Flow Case

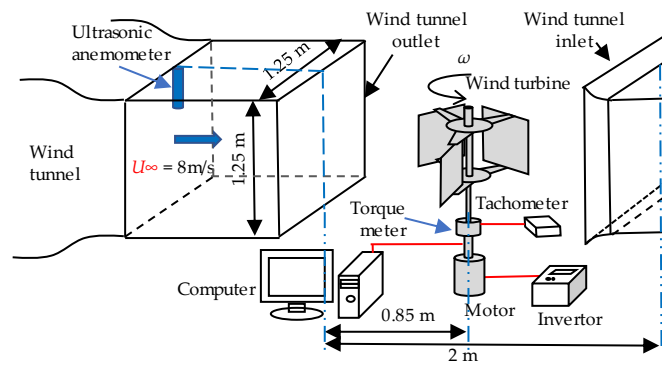
Figure 3a shows the experimental setup for the uniform flow case. The experiments were conducted using a closed circuit wind tunnel with an open test section. The size of the cross section of the wind tunnel outlet was 1.25 m × 1.25 m. The blockage ratio which is defined as the ratio of the projected rotor's swept area to the wind tunnel outlet area was approximately 18%. The O-VAWT was set in the test section so that the rotor center was at the center of the cross-section of the wind tunnel outlet and 0.850 m downwind of the wind tunnel outlet. Here, we defined the rotor center as the point on the rotational axis of the rotor and at the mid-height of the blades. In addition, we set the origin of the coordinate system at the rotor center, as shown in Figure 2c,d. The rotor was driven by a motor (Mitsubishi Electric, GM-S) and its rotational speed (ω) was monitored by using a digital tachometer (Ono Sokki, HT-5500) and controlled by using an inverter (Hitachi, SJ200). The rotor torque was measured by using a torque meter (TEAC, TQ-AR), which was connected to the motor and shaft via couplings. The output signal of the torque meter was converted by a 16-bit analog-to-digital converter with a sampling interval of 0.5°, and 36,000 items (50 revolutions) of data were stored. To measure the reference wind speed U_∞ , an ultrasonic anemometer (Kaijo Sonic, DA-650-3TH and TR-90 AH) was set approximately 2 m upwind of the wind tunnel outlet. The value of U_∞ was kept at 8 m/s. The value of tip speed ratio λ , which is defined as:

$$\lambda = R\omega/U_\infty, \quad (3)$$

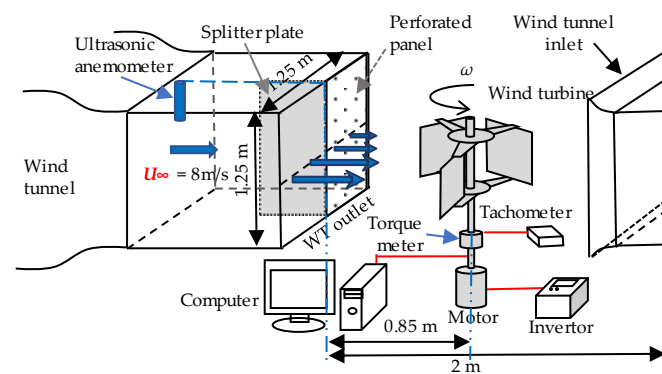
was varied from 0.1 to 0.8 with an increment of 0.1.

2.3. Experimental Setup for Shear Flow Cases

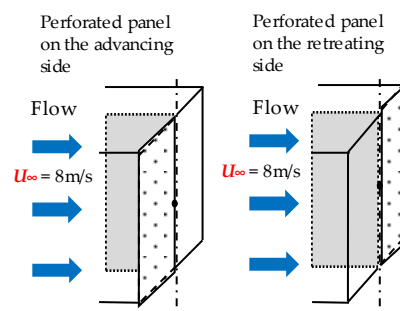
To generate a horizontal shear flow, a perforated panel and a splitter plate were installed at the outlet of the wind tunnel as shown in Figure 3b,c and Figure 4. The perforated panel had a width of 1.0 m, a height of 1.5 m and a thickness of 2×10^{-3} m, and was set so that it covered half of the wind tunnel outlet in the horizontal wind direction. Due to the existence of the perforated panel, the pressure upwind of the panel increased and the wind flow rate through the wind-tunnel-outlet area covered by the panel decreased while that through the uncovered wind-tunnel-outlet area increased. When the perforated panel covered the wind-tunnel-outlet area upwind of the retreating side of the rotor, the wind speed of the generated shear flow was higher on the advancing side of the rotor. Hereafter, this type of shear flow is referred to as "advancing side faster shear flow" (ASF-SF). On the other hand, when the perforated panel covered the wind-tunnel-outlet area upwind of the advancing side of the rotor, the wind speed of the generated shear flow was higher on the retreating side of the rotor. Hereafter, this type of shear flow is referred to as "retreating side faster shear flow" (RSF-SF). The splitter plate was set vertically, parallel to the wind tunnel wall and at the center of the wind tunnel outlet to avoid the horizontal component of the wind velocity in the generated shear flow becoming significant. The splitter plate had a width of 0.88 m, a height of 1.25 m and a thickness of 4×10^{-3} m.



(a)



(b)



(c)

Figure 3. The experimental apparatus and measurement devices; (a) in uniform flow, (b) in shear flows and (c) the porous plate position at the nozzle exit of the wind tunnel in case of shear flows.

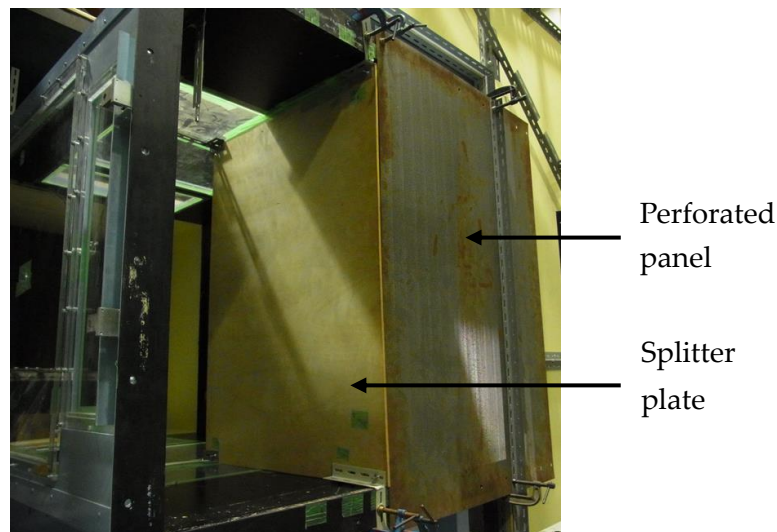


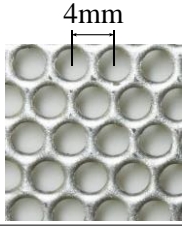
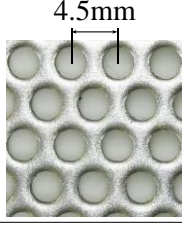
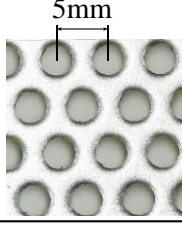
Figure 4. The perforated panel and splitter plate set at the outlet of the wind tunnel.

To investigate the effects of the strength of the shear flow on the performance of the O-VAWT, we generated three kinds of shear flows by using three perforated panels shown in Table 1. With regard to a staggered round-hole perforated panel, the shielding ratio Φ , which is the ratio of the area that shields the airflow to the whole area of the perforated panel, can be computed by:

$$\Phi = 1 - \frac{\pi d^2}{2\sqrt{3} L^2}, \tag{4}$$

where d is a diameter of a hole and L is the distance between the centers of adjacent holes.

Table 1. Perforated panels. Here, d is the diameter of a hole, L is the distance between the centers of adjacent holes and Φ is the shielding ratio.

| Name | d [m] | L [m] | Φ [-] | Enlarged View |
|--------------------|--------------------|----------------------|------------|---|
| Perforated panel A | 3×10^{-3} | 4×10^{-3} | 0.49 |  |
| Perforated panel B | 3×10^{-3} | 4.5×10^{-3} | 0.60 |  |
| Perforated panel C | 3×10^{-3} | 5×10^{-3} | 0.67 |  |

Except for the installation of the perforated panels and the splitter plate, the experimental setup for the measurement of the performance of the O-VAWT was the same as the uniform flow case. Prior to the measurement of the performance of the O-VAWT, we measured the horizontal profiles of the generated shear flows at 0.10 m downwind of and at the center height of the wind tunnel outlet by using an x-type hot-wire probe (Kanomax, 0252R-T5).

2.4. Torque and Power Coefficients

Due to the difficulty of evaluating the mechanical losses of the bearings, the sprockets and the chains, this study considers only the aerodynamic torque generated by the blades as the rotor torque of the O-VAWT. The aerodynamic torque generated by the blades was computed by:

$$T_B = T_{wB} - T_{woB}, \quad (5)$$

where T_{wB} was the measured aerodynamic torque generated by the rotor when the blades were not removed; and T_{woB} was the measured aerodynamic torque generated by the rotor when the blades were removed. It is worth noting that, generally, when the blades were not removed from the rotor, the rotor generated positive torque while the motor acted as a load to keep the value of ω constant. Conversely, at all tip speed ratios, when the blades were removed from the rotor, the rotor generated negative torque while the motor acted as the driving force of the rotor revolution. Therefore, at all tip speed ratios, T_B was higher than T_{wB} .

The power coefficient describes that fraction of the power in the wind that may be converted by the turbine into mechanical work [30] and is defined in this study as:

$$C_P = \frac{T_B \omega}{0.5 \rho A U_0^3}, \quad (6)$$

and the torque coefficient is defined as:

$$C_T = \frac{T_B}{0.5 \rho A U_0^2 R}. \quad (7)$$

Here, the U_0 is the time-mean stream-wise velocity, $\bar{u}(x, y, z)$, averaged over the projected rotor's swept area at $x = 0$ and is computed by:

$$U_0 = \frac{\int_{-(R+0.5c)}^R \bar{u}(0, y, 0) dy}{2R+0.5c}. \quad (8)$$

3. Numerical Approach

The CFD software utilized to simulate the wind flow field was ANSYS Fluent 17.2 [31,32]. The numerical approach was based on our previous paper [22,33], in which the CFD simulations with the delayed detached eddy simulation (DDES) turbulence model of flow around the O-VAWT were conducted and the validities of the grid resolution and the time-step size were confirmed.

3.1. Governing Equations and Discretization Method

The flow field around the wind turbine was assumed to be incompressible and isothermal. The DDES turbulence mode treats near-wall region in a manner like a Reynolds-averaged Navier–Stokes (RANS) turbulence model and treats the rest of the flow field in a manner like a large-eddy simulation (LES) turbulence model [34]. This model has the potential to achieve higher accuracy than RANS models and save a large number of computing resources compared with pure LES models. The governing equations for the CFD simulation with the DDES turbulence model based on the Spalart–Allmaras (SA) model are the continuity equation:

$$\frac{\partial u_i}{\partial x_i} = 0, \tag{9}$$

the Navier–Stokes equation:

$$\frac{\partial u_i}{\partial t} + \frac{\partial u_i u_j}{\partial x_j} = -\frac{1}{\rho} \frac{\partial p}{\partial x_i} + \nu \frac{\partial}{\partial x_j} \left(\frac{\partial u_i}{\partial x_j} + \frac{\partial u_j}{\partial x_i} - \frac{2}{3} \delta_{ij} \frac{\partial u_i}{\partial x_j} \right) - \frac{\partial}{\partial x_j} \left[\tilde{\nu} \left(\frac{\partial u_i}{\partial x_j} + \frac{\partial u_j}{\partial x_i} \right) - \frac{2}{3} k \delta_{ij} \right], \tag{10}$$

and the transport equation for the kinematic eddy viscosity $\tilde{\nu}$:

$$\frac{\partial \tilde{\nu}}{\partial t} + \frac{\partial \tilde{\nu} u_i}{\partial x_i} = C_{b1} \tilde{\nu} \left(S + \frac{\tilde{\nu}}{\kappa^2 d_{DDES}^2} \left(1 - \frac{\chi}{1 + \chi f_{v1}} \right) \right) + \frac{1}{\sigma_{\tilde{\nu}}} \left[\frac{\partial}{\partial x_j} \left\{ (\nu + \tilde{\nu}) \frac{\partial \tilde{\nu}}{\partial x_j} \right\} + C_{b2} \left(\frac{\partial \tilde{\nu}}{\partial x_j} \right)^2 \right] - C_{w1} f_w \left(\frac{\tilde{\nu}}{d_{DDES}} \right)^2 \tag{11}$$

where u_i is the wind-velocity component in the x_i direction; p is the pressure; ν is the kinematic viscosity; t is the time; ρ is the air density; k is the turbulence kinetic energy; δ_{ij} is the Kronecker delta; d_{DDES} is the DDES length scale; χ is $(\tilde{\nu}/\nu)$; S is a scalar measure of the deformation tensor; f_{v1} and f_w are damping functions; and C_{b1} , C_{b2} , C_{w1} , $\sigma_{\tilde{\nu}}$ and κ are constants.

The DDES length scale is computed by:

$$d_{DDES} = d - f_d \max(0, d - c_{des} \Delta_{max}) \tag{12}$$

where d is the distance to the closest wall; c_{des} is the empirical constant; and Δ_{max} is the maximum edge length of the local computational cell, i.e., $\Delta_{max} = \max(\Delta_x, \Delta_y, \Delta_z)$. The switching between the RANS and the LES mode depends on the following shielding function;

$$f_d = 1 - \tanh\left((8r_d)^3\right) \tag{13}$$

and

$$r_d = \frac{\tilde{\nu}}{\sqrt{u_{i,j} u_{i,j} \kappa^2 d^2}} \tag{14}$$

where $u_{i,j}$ is the velocity gradient. The damping functions and closure coefficients are as follows:

$$f_{v1} = \frac{\chi^3}{c_{v1}^3 + \chi^3}, f_w = g \left[\frac{1 + c_{w3}^6}{g^6 + c_{w3}^6} \right]^{1/6}, g = r + c_{w2}(r^6 - r), c_{w1} = \frac{c_{b1}}{\kappa^2} + \frac{(1 + c_{b2})}{\sigma_{\tilde{\nu}}}, \tag{15}$$

$$c_{b1} = 0.1355, c_{b2} = 0.622, c_{v1} = 7.1, c_{w2} = 0.3, c_{w3} = 2.0, \sigma_{\tilde{\nu}} = \frac{2}{3}, c_{des} = 0.65, \kappa = 0.4187. \tag{16}$$

The governing equations are discretized by the finite-volume method. The advection terms of the Navier–Stokes equations are discretized by the bounded central-difference scheme. The advection term of the transportation equations for $\tilde{\nu}$ is discretized by a second-order upwind scheme. Other spatial derivatives are discretized by the central-difference scheme. The time integration is performed using the second-order implicit method.

3.2. Numerical Setup

The computational domain, the computational meshes and the boundary conditions are shown in Figure 5. As the same as the experimental setup, the origin of the coordinate system is defined at the center of the O-VAWT. The modeled O-VAWT was comprised of three blades, one main shaft and two sets of connecting arms. To reduce the computational cost, other components, such as the chains and sprockets are omitted. The sizes of these components are the same as those used in the experiment. The computational domain consists of three blade domains, one rotor domain and one far-field domain. The blade domain included one of the blades and rotates around each blade axis. The rotor domain

included these three blade domains, the main shaft and the connecting arms and rotates around the main shaft. The far-field domain was a stationary domain and its size was $23.5D \times 17D \times 5D$. Except for uniform flow cases, a splitter plate with the same thickness as the experiment was set at $y = 0$ and $x = -11.37D$ to $-1.67D$. In all domains, only unstructured meshes were used. Based on our previous mesh-resolution dependency tests [33], the number of computational cells in each domain were set as shown in Table 2. The total number of computational cells was approximately 10 million. All surfaces of the solid components were covered with boundary-layer meshes. The first grid nodes over the surface of the blades were $y^+ < 1$ in all run cases.

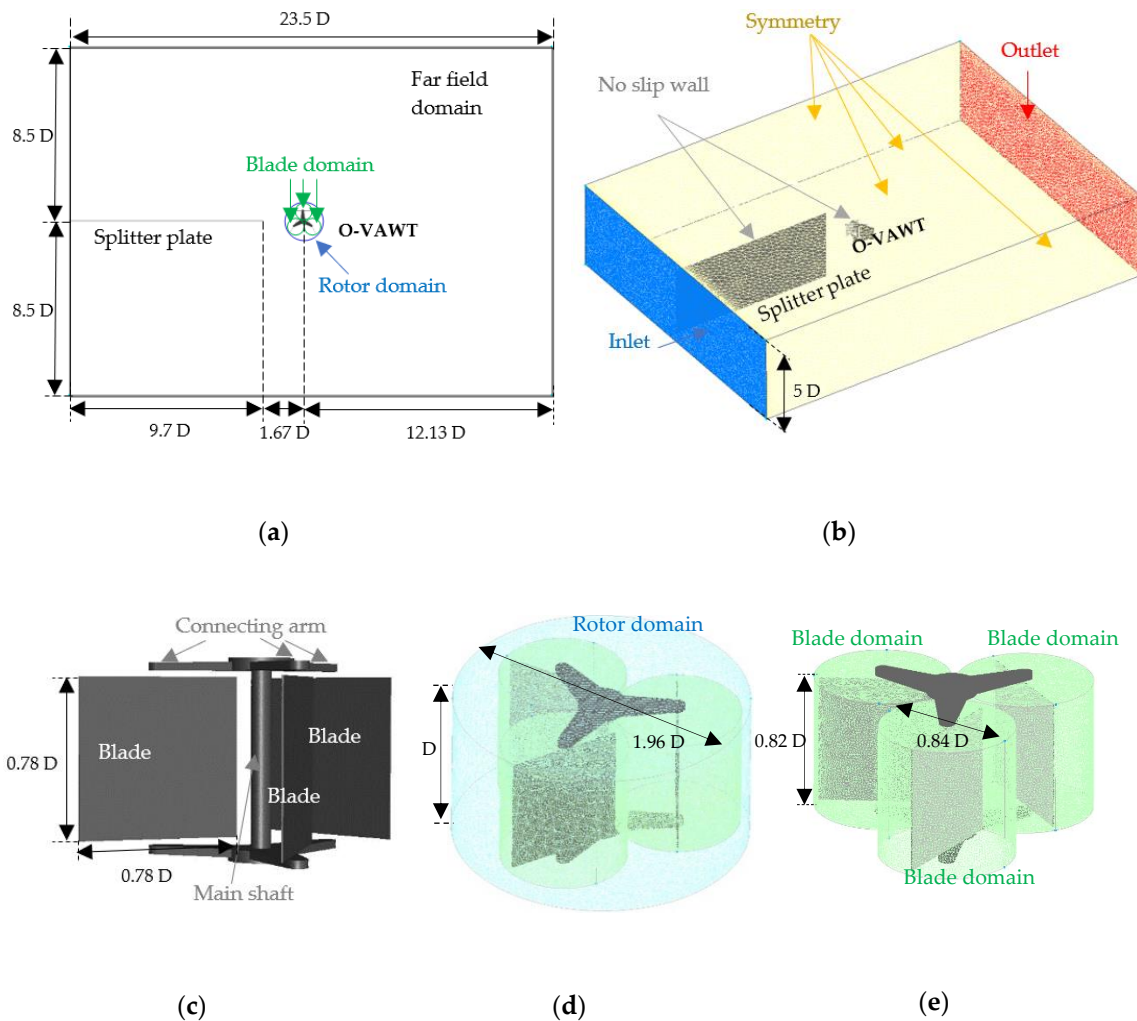


Figure 5. Computational domain, computational mesh and boundary conditions. (a) Top view of the computational domain; (b) bird’s eye view of the computational domain with computational mesh and boundary conditions; (c) modeled rotor; (d) blade domains and (e) rotor domain.

Table 2. Numbers of grid sizes.

| Domain | Mesh on This Research | Regular Mesh Used by ElCheikh [33] |
|--------------|-----------------------|------------------------------------|
| Blade 1 | 2,300,530 | 1,610,660 |
| Blade 2 | 2,303,725 | 1,614,903 |
| Blade 3 | 2,304,607 | 1,588,363 |
| Blade 4 | - | 1,614,661 |
| Rotor | 1,756,635 | 2,127,497 |
| Far end | 1,770,583 | 441,196 |
| TOTAL | 10,436,080 | 8,997,280 |

At the inlet boundary, the distributions of the stream-wise wind velocity shown in Table 3 were implemented. These distributions were set so that when the O-VAWT is absent, the distributions of the time-mean values of u at $x \approx -0.147 D$, which corresponds to 0.1 m downwind of the wind tunnel outlet, matched well with those of the wind tunnel experiment, which were generated by using the three kinds of perforated panels with different shielding ratios Φ , as shown in Figure 6a,b. Here, U_H and U_L are the maximum and minimum streamwise velocities in the profile of a shear flow measured in the wind tunnel experiment; Γ is the velocity ratio defined as:

$$\Gamma = \frac{U_H - U_L}{U_H + U_L} \tag{17}$$

Table 3. Distribution of u at the inlet boundary. Here, Γ is the velocity ratio; Φ is the shielding ratio of a perforated panel; U_H and U_L are the maximum and minimum velocities in a shear flow.

| Flow Type | Γ | Φ | U_H [m/s] | Range of U_H Region [m] | Velocity Distribution in Transition Region | Range of Transition Region [m] | U_L [m/s] | Range of U_L Region [m] |
|-----------|----------|--------|-------------|---------------------------|--|--------------------------------|-------------|---------------------------|
| Uniform | 0 | - | 8 | | 8 | | 8 | |
| ASF-SF | 0.51 | 0.67 | 13.2 | $y \leq -0.24$ | $U_H \cdot (-y/0.24)^{0.3}$ | $-0.24 \leq y \leq -0.01$ | 4.3 | $y \geq -0.01$ |
| ASF-SF | 0.40 | 0.60 | 12.1 | $y \leq -0.22$ | $U_H \cdot (-y/0.22)^{0.35}$ | $-0.22 \leq y \leq 0.02$ | 5.2 | $y \geq -0.02$ |
| ASF-SF | 0.28 | 0.49 | 10.8 | $y \leq -0.18$ | $U_H \cdot (-y/0.18)^{0.2}$ | $-0.18 \leq y \leq -0.01$ | 6.1 | $y \geq -0.01$ |
| RSF-SF | 0.51 | 0.67 | 13.2 | $y \geq 0.24$ | $U_H \cdot (y/0.24)^{0.3}$ | $0.01 \leq y \leq 0.24$ | 4.3 | $y \leq 0.01$ |
| RSF-SF | 0.40 | 0.60 | 12.1 | $y \geq 0.22$ | $U_H \cdot (y/0.24)^{0.35}$ | $0.02 \leq y \leq 0.22$ | 5.2 | $y \leq 0.02$ |
| RSF-SF | 0.28 | 0.49 | 10.8 | $y \geq 0.18$ | $U_H \cdot (y/0.24)^{0.2}$ | $0.01 \leq y \leq 0.18$ | 6.1 | $y \leq 0.01$ |

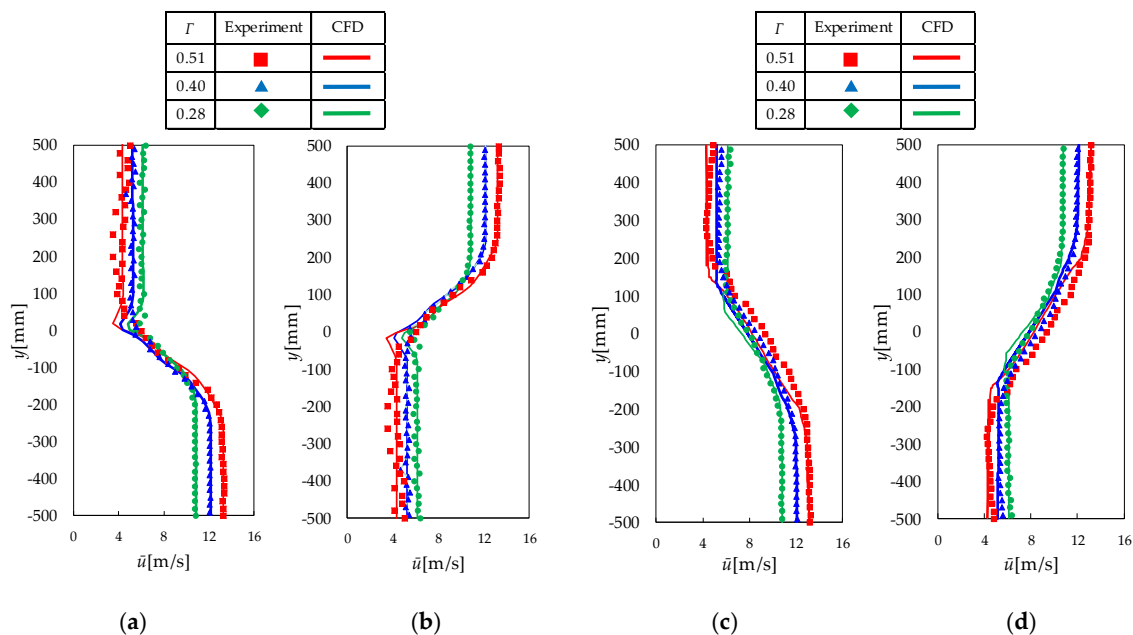


Figure 6. Horizontal distribution of the time-mean values of streamwise velocity at the mid-height of the wind tunnel outlet at $x \approx -0.147D$, which corresponds to 0.1 m downwind of the wind tunnel outlet, and $x = 0$, which corresponds to the position of the rotational axis of the O-VAWT, when the O-VAWT is absent. (a) ASF-SF cases at $x \approx -0.147D$, (b) RSF-SF cases at $x \approx -0.147D$, (c) ASF-SF cases at $x = 0$ and (d) RSF-SF cases $x = 0$.

It is worth noting that amplification factors of $\Gamma = 0.28$ and $\Gamma = 0.51$ are considered as 1.35 and 1.65, respectively, by computing U_H/U_∞ . The amplification factor is defined as the ratio of wind speed in the case where there are buildings to wind speed in the case where these buildings are removed.

The separated shear flow from a building with an aspect ratio of 1:1:2 reaches an amplification factor of 1.2 [35]. In addition, the separated shear flow from a building with an aspect ratio of 1:1:6 reaches an amplification factor of 1.7 [36]. At $x = 0$, the values of Γ do not change, as shown in Figure 6c,d. However, due to the momentum diffusion, the horizontal gradients of the time-mean streamwise velocity become weaker. One of the reasons for the relatively large discrepancies between the profiles obtained by the experiment and the CFDs can be that the turbulence intensities of the CFDs are significantly small compared to those of the experiments, as shown in Figure 7. Even though very high values of turbulence intensity were set at the inlet boundary, the turbulence intensities dissipated rapidly and became very small at $x = 0$ as compared to those of the experiments. As the setting of high turbulence intensity at the inlet boundary leads to computational instability, we set no perturbation condition at the inlet boundary. Table 4 shows the values of U_0 computed by Equation (8) and the Reynolds number which is defined as:

$$Re = \frac{U_0 D}{\nu} \tag{18}$$

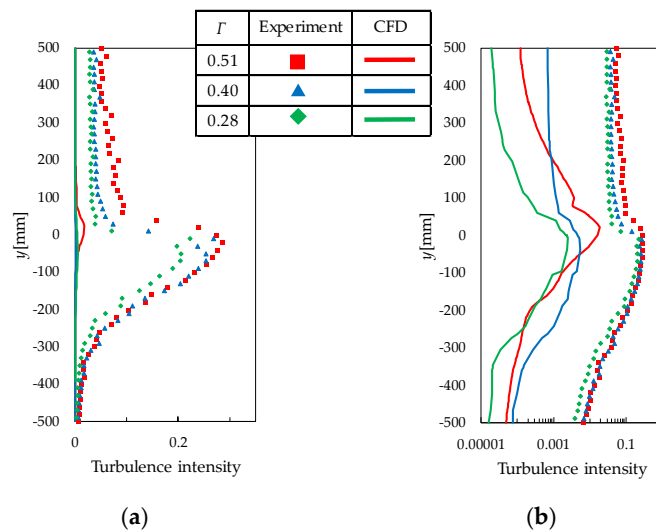


Figure 7. Horizontal distribution of the turbulence intensity of ASF-SF cases at the mid-height of the wind tunnel outlet at $x = 0$, which corresponds to the position of the rotational axis of the O-VAWT, when the O-VAWT was absent. (a) Linear scale on the horizontal axis and (b) logarithmic scale in the horizontal axis.

Table 4. Experimental and computational fluid dynamics (CFD) results for the values of U_0 and Re for the uniform flow, ASF-SF and RSF-SF cases.

| Flow Type | Γ | U_0 [m/s] | | Re | |
|-----------|----------|-------------|------|--------------------|--------------------|
| | | Experiment | CFD | Experiment | CFD |
| Uniform | 0 | 8 | 8 | 2.79×10^5 | 2.79×10^5 |
| ASF-SF | 0.51 | 10.08 | 9.78 | 3.52×10^5 | 3.41×10^5 |
| ASF-SF | 0.40 | 9.38 | 9.22 | 3.28×10^5 | 3.22×10^5 |
| ASF-SF | 0.28 | 8.73 | 8.72 | 3.05×10^5 | 3.05×10^5 |
| RSF-SF | 0.51 | 7.76 | 7.48 | 2.71×10^5 | 2.61×10^5 |
| RSF-SF | 0.40 | 7.72 | 7.36 | 2.70×10^5 | 2.57×10^5 |
| RSF-SF | 0.28 | 7.52 | 7.33 | 2.62×10^5 | 2.56×10^5 |

At the outlet boundary, the pressure outlet condition with $p = 0$ was imposed. On the surface of the O-VAWT and the splitter plate, the no-slip boundary conditions were set. The sliding mesh technique was used to couple the rotational domains and the stationary domain. The direction of the rotor and the blade rotations are counterclockwise and clockwise, respectively, when viewed from the

top (Figure 5a). By changing the rotational speed of the rotor ω , the tip speed ratio λ was set at 0.2, 0.4, 0.5, 0.6, or 0.8. The time step sizes were set as $dt = 0.5^\circ/\omega$.

3.3. Torque and Power Coefficients

As mentioned in sub-Section 2.4, this study considers only the aerodynamic torque generated by the blades as the rotor torque of the O-VAWT. Since each of the blade axes was connected with the main shaft by a chain via sprockets, the aerodynamic torque on each of the blades about each of the blade axes was transmitted through the chain and contributed to the torque about the main shaft. Therefore, the rotor torque generated by a blade at an azimuthal angle φ is expressed as:

$$T_B(\varphi) = T_{B_rev}(\varphi) + T_{B_rot}(\varphi), \quad (19)$$

where $T_{B_rev}(\varphi)$ is the conventional blade torque that is calculated by multiplying the rotor radius and the component of the aerodynamic force on the blade at φ in the rotor-revolution direction; and $T_{B_rot}(\varphi)$ is the torque generated by the component of the aerodynamic force on the blade at φ in the blade-rotation direction about the blade axis. Hereafter, we call $T_B(\varphi)$ the “blade torque,” $T_{B_rev}(\varphi)$ the “rotor-revolution torque” and $T_{B_rot}(\varphi)$ the “blade-rotation torque.” The blade torque coefficient (C_{TB}), the rotor-revolution component (C_{TB_rev}) and the blade-rotation component (C_{TB_rot}) are defined as:

$$C_{TB}(\varphi) = \frac{T_B(\varphi)}{0.5\rho AU_0^2 R}, \quad (20)$$

$$C_{TB_rev}(\varphi) = \frac{T_{B_rev}(\varphi)}{0.5\rho AU_0^2 R}, \quad (21)$$

and

$$C_{TB_rot}(\varphi) = \frac{T_{B_rot}(\varphi)}{0.5\rho AU_0^2 R}. \quad (22)$$

It should be noted that C_{TB} , C_{TB_rev} and C_{TB_rot} are coefficients of one blade.

The CFD simulations were conducted for eight revolutions of the rotor. Using the data of the last two rotor revolutions, the torque coefficient C_T was computed by the following formula:

$$C_T = \frac{n}{N_e - N_s} \sum_{N=N_s+1}^{N_e} \int_0^{2\pi} C_{TB} d\varphi. \quad (23)$$

Here, n ($= 3$) is the number of the blades; N_s ($= 6$) is the number of the rotor revolutions before starting the computation of C_T ; N_e ($= 8$) is the number of the rotor revolutions before finishing the computation of C_T . The power coefficient of C_P was computed by Equation (6).

4. Results and Discussion

In this section, the results of the wind tunnel experiments and the CFD simulations for the power performance of the O-VAWT, such as the dependency of the power and torque coefficients on the tip speed ratio, the variations of the torque coefficients with azimuthal angle, are presented for the uniform flow case and the shear flow cases. Subsequently, the causes of the features of the power performance of the O-VAWT are discussed based on the CFD results of the flow fields.

4.1. Performance in Uniform Flow

Figure 8a shows the power and torque coefficients (C_P and C_T) of the O-VAWT in the uniform flow. The CFD results are in good agreement with the experimental ones. The optimal tip speed ratio at which C_P becomes the maximum is less than unity; 0.4 in the experiments and 0.5 in the

CFD simulations. As mentioned in the introduction, this low optimal tip speed ratio is a favorable feature for the built environment from the viewpoint of aerodynamic noise. With increasing λ , C_T decreases monotonically from a small tip speed ratio ($\lambda = 0.2$). These tendencies are commonly found among drag-type wind turbines. The wind-tunnel experimental results by Shimizu et al. [24] for C_P and C_T of an O-VAWT with two elliptical cross-sectional blades show the same tendencies as our results. The value of the maximum C_P is 0.32 in our experiments and CFD simulations, while the value is 0.176 in Shimizu et al.'s experiments. The main factors for the better performance of our O-VAWT as compared to Shimizu et al.'s O-VAWT can be the number of blades and the cross-sectional shape of the blades. In our previous studies, the maximum C_P improved from 0.189 to 0.244 by changing the number of blades from two to three [33] and improved from 0.246 to 0.288 by changing the cross-sectional shape of blades from ellipse to rectangle [23].

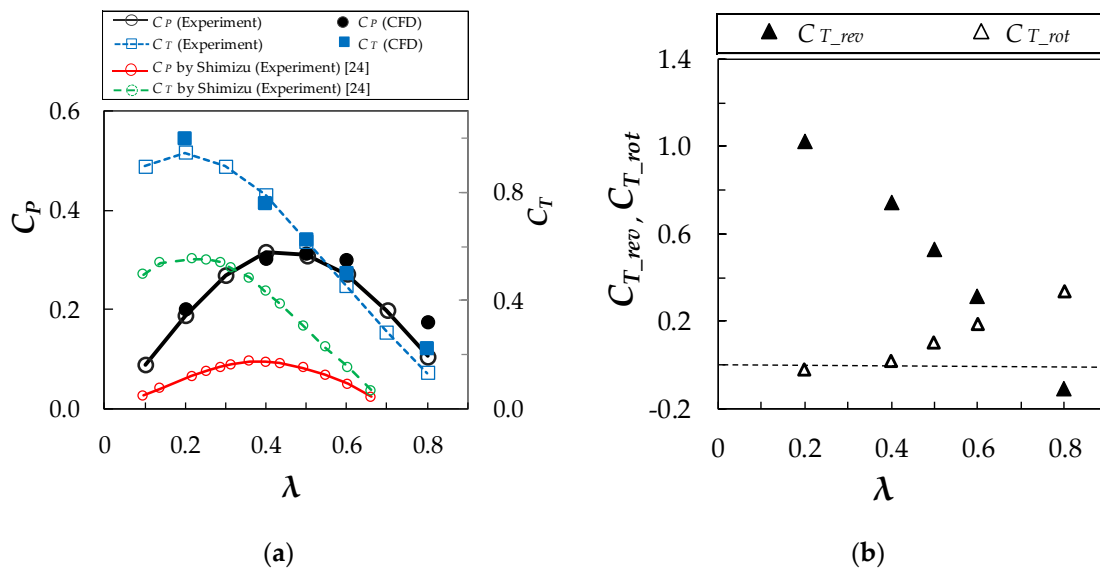


Figure 8. Performance of the O-VAWT in the uniform flow; (a) the variation of power coefficient (C_P) and torque coefficient (C_T) with tip speed ratios (λ) by the experiments and CFD simulations, (b) rotor-revolution (C_{T_rev}) and blade-rotation (C_{T_rot}) components of torque coefficients (C_T) computed by the CFD simulations. The wind-tunnel experimental results by Shimizu et al. [24] for C_P and C_T of an O-VAWT with two elliptical cross-sectional blades are added for reference.

Figure 8b shows C_{T_rev} and C_{T_rot} computed by the CFD results. The sum of C_{T_rev} and C_{T_rot} is C_T . As well as C_T , the value of C_{T_rev} decreases monotonically with an increase in λ . Conversely, the value of C_{T_rot} increases with an increase in λ . The values of C_{T_rev} are positive and larger than those of C_{T_rot} except for $\lambda = 0.8$. At $\lambda = 0.8$, C_{T_rev} is negative; however, C_{T_rot} is positive and its absolute value is larger than that of C_{T_rev} . As a result, C_T is positive at $\lambda = 0.8$.

Figure 9 shows the variations of blade torque coefficient (C_{TB}), its rotor-revolution component (C_{TB_rev}) and blade-rotation component (C_{TB_rot}) with respect to azimuthal angle (φ) at $\lambda = 0.4$ and 0.6 . The value of C_{TB} is significantly large in the upwind region of the advancing side ($\varphi \approx 180^\circ$ to 270°) of the rotor, being the maximum at $\varphi \approx 210^\circ$. In the range of φ where C_{TB} is significantly large, the contribution of C_{TB_rev} is dominant. Except for this range, C_{TB_rev} does not always positively contribute to C_{TB} . At φ where the value of C_{TB_rev} is negative, the value of C_{TB_rot} is generally positive and the rotation of the blade positively contributes to C_{TB} . Due to this positive contribution of C_{TB_rot} to C_{TB} , the value of C_{TB} is positive at almost all φ and the variation of C_{TB} of the O-VAWT with respect to φ is smaller as compared to that of a Savonius-type VAWT. The variation of C_{TB} of a Savonius-type VAWT with respect to φ in Figure 9 is a result of CFD simulation by Tian et al. [37]. The maximum C_P and the optimal λ of the Savonius-type VAWT were 0.258 and 1.0, respectively.

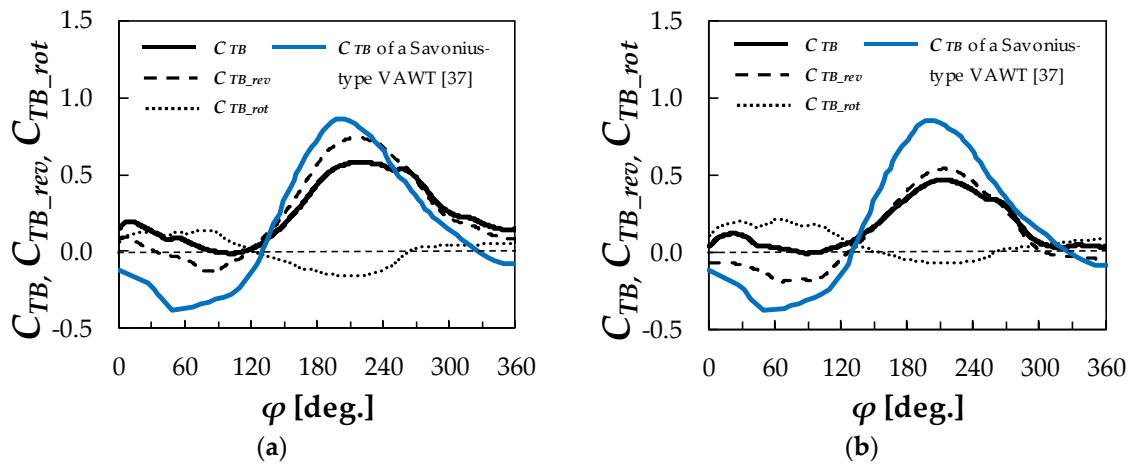


Figure 9. The variation of blade torque coefficients (C_{TB}), its rotor-revolution component (C_{TB_rev}) and its blade-rotation component (C_{TB_rot}) with azimuthal angle (φ) at; (a) $\lambda = 0.4$ and (b) $\lambda = 0.6$. Note that C_{TB} , C_{TB_rev} and C_{TB_rot} are coefficients of one blade. The CFD simulation result by Tian et al. [37] for the variation of C_{TB} of a Savonius-type VAWT with φ is added for comparison.

4.2. Performance in Shear Flows

Figure 10 compares the experimental results for C_p of the O-VAWT in the cases of the advancing side faster shear flow (ASF-SF), the retreating side faster shear flow (RSF-SF) and the uniform flow. In the cases of the ASF-SF, C_p is higher than in the case of the uniform flow at all λ and increases with an increase in Γ . In the cases of the RSF-SF, similar to the cases of the ASF-SF, C_p increases with an increase in Γ . However, when $\Gamma = 0.28$, the values of C_p are lower than those of the uniform flow case. Concerning the optimal λ , there is a trend that it shifts to higher λ in both cases of shear flows as compared to the uniform flow case, except for the RSF-SF with $\Gamma = 0.28$.

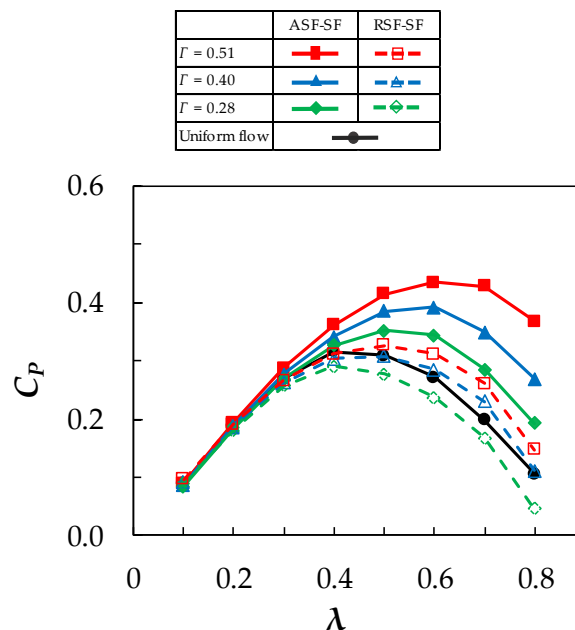


Figure 10. Power coefficient (C_p) of O-VAWT in shear flows by the experiments.

Both in the cases of the ASF-SF (Figure 11a) and the RSF-SF (Figure 11b), the CFD results for C_p - λ curves are in good agreement with the experimental ones. In the following discussion, we use the CFD results for the torque of the O-VAWT and the flow field to explain the effects of shear flows on the characteristics of the power performance.

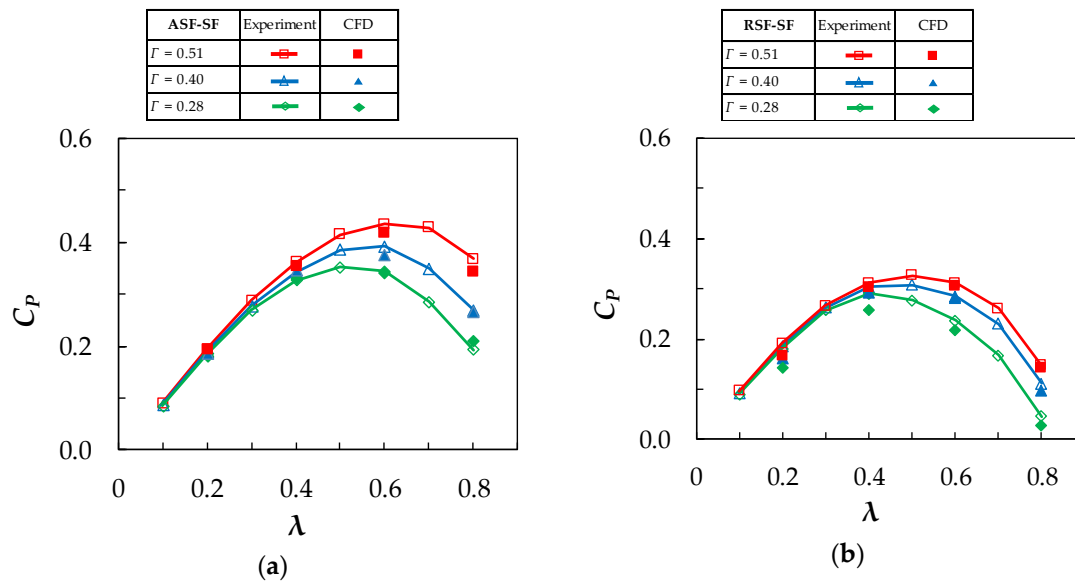


Figure 11. Power coefficient (C_p) of O-VAWT in shear flows by the experiments and the CFD simulations in the cases of; (a) the ASF-SF and (b) the RSF-SF.

Figure 12 shows the variations of blade torque coefficient (C_{TB}), its rotor-revolution component ($C_{TB_{rev}}$) and its blade-rotation component ($C_{TB_{rot}}$) with azimuthal angle (φ) in the cases of the ASF-SF. It is confirmed that these profiles are qualitatively the same between the cases of $\lambda = 0.4$ and $\lambda = 0.6$. Therefore, it is considered that the effects of the shear flow on the characteristics of the blade torque variations with φ do not significantly change around the optimal λ . As compared to the case of the uniform flow, C_{TB} is higher on most of the advancing side of the rotor ($\varphi \approx 210^\circ$ to 330°) and lower in the upwind region of the retreating side of the rotor, specifically at $\varphi \approx 120^\circ$ to 150° . In particular, with an increase in Γ , C_{TB} increases on most of the advancing side of the rotor ($\varphi \approx 210^\circ$ to 330°). The optimal φ at which C_{TB} is the maximum shifts to the downwind direction on the advancing side of the rotor ($\varphi \approx 240^\circ$) as compared to the case of the uniform flow. The effects of the shear flow on the variations of $C_{TB_{rev}}$ with φ is almost the same as C_{TB} . As compared to the case of the uniform flow, $C_{TB_{rev}}$ is higher on most of the advancing side of the rotor ($\varphi \approx 210^\circ$ to 330°). In contrast, $C_{TB_{rot}}$ is lower in most of the upwind region of the advancing side ($\varphi \approx 180^\circ$ to 240°) and slightly higher in the upwind region of the retreating side of the rotor, specifically at 120° to 150° as compared to the case of the uniform flow. With an increase in Γ , $C_{TB_{rot}}$ decreases in the upwind region of the advancing side of the rotor ($\varphi \approx 180^\circ$ to 240°). Due to its negative values of $C_{TB_{rot}}$, the optimal φ at which C_{TB} is the maximum slightly shifts to the downwind direction as compared to $C_{TB_{rev}}$.

Figure 13 shows the variation of blade torque coefficient (C_{TB}), its rotor-revolution component ($C_{TB_{rev}}$) and its blade-rotation component ($C_{TB_{rot}}$) with azimuthal angle (φ) in the cases of the RSF-SF. Since these profiles are qualitatively the same between the cases of $\lambda = 0.4$ and $\lambda = 0.6$, it is considered that the effects of the shear flow on the characteristics of the blade torque variations with φ do not significantly change around the optimal λ . As compared to the case of the uniform flow, C_{TB} is significantly higher in most of the upwind region of the retreating side ($\varphi \approx 120^\circ$ to 180°) and lower on most of the advancing side of the rotor ($\varphi \approx 210^\circ$ to 330°). In particular, with an increase in Γ , C_{TB} increases in the upwind region of the retreating side of the rotor. The optimal φ at which C_{TB} is the maximum shifts to the upwind region of the retreating side of the rotor ($\varphi \approx 150^\circ$) as compared to the case of the uniform flow. The effects of the shear flow on the variation of $C_{TB_{rev}}$ with φ is almost the same as C_{TB} . As compared to the case of the uniform flow, $C_{TB_{rev}}$ is higher in most of the upwind region of the retreating side ($\varphi \approx 100^\circ$ to 160°) and lower on most of the advancing side of the rotor ($\varphi \approx 210^\circ$ to 330°). In contrast, $C_{TB_{rot}}$ is slightly lower in most of the upwind region of the retreating side ($\varphi \approx 90^\circ$ to 150°) and slightly higher in most of the upwind region of the advancing side of the

rotor ($\varphi \approx 180^\circ$ to 240°) as compared to the case of the uniform flow. Furthermore, with an increase in Γ , C_{TB_rot} decreases in most of the upwind region of the retreating side ($\varphi \approx 100^\circ$ to 160°) and increases in most of the upwind region of the advancing side of the rotor ($\varphi \approx 180^\circ$ to 240°).

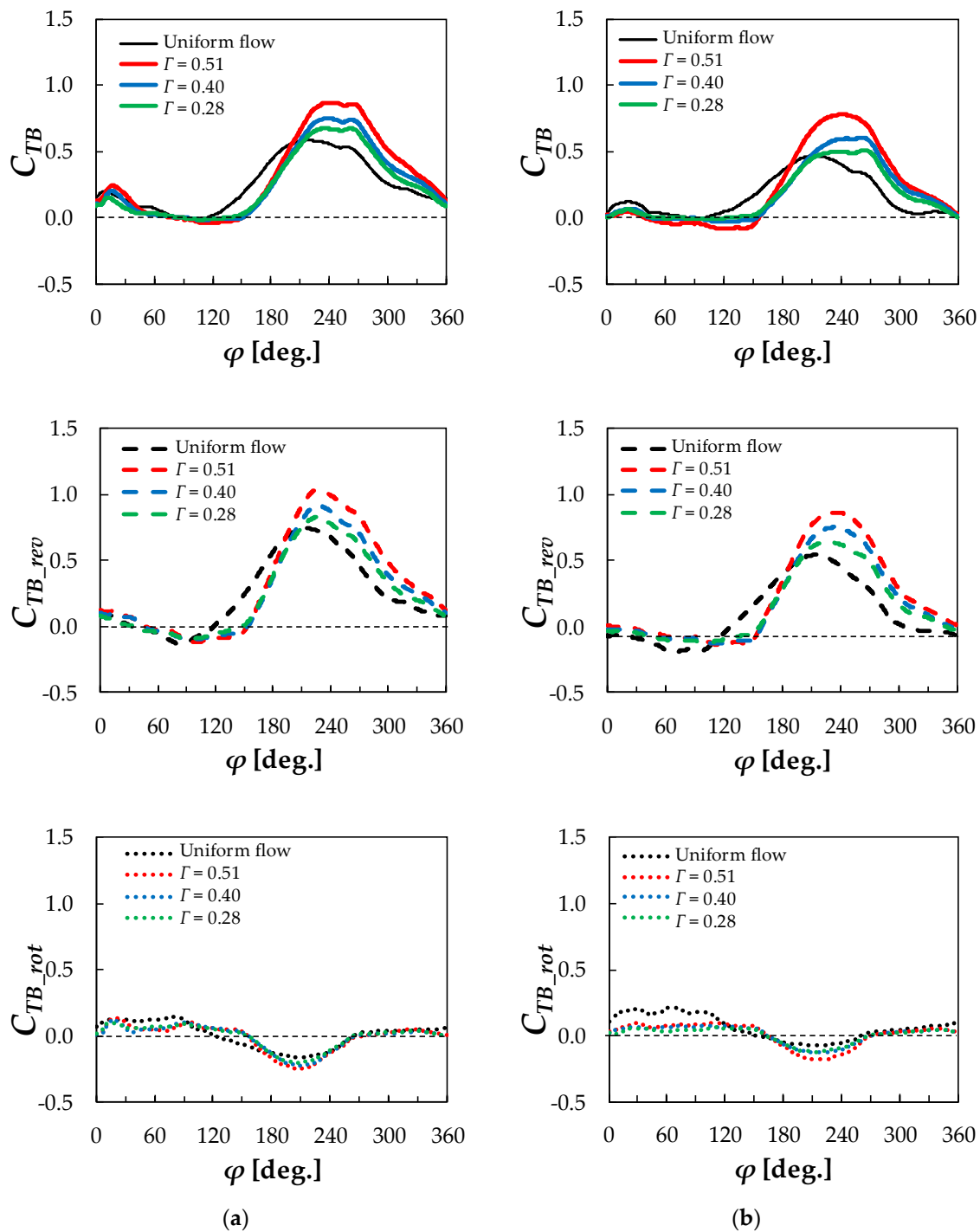


Figure 12. The variation of blade torque coefficient (C_{TB}), its rotor-revolution component (C_{TB_rev}) and its blade-rotation component (C_{TB_rot}) in the cases of the ASF-SF computed by the CFD simulations; (a) for $\lambda = 0.4$ and (b) for $\lambda = 0.6$. Note that C_{TB} , C_{TB_rev} and C_{TB_rot} are coefficients of one blade.

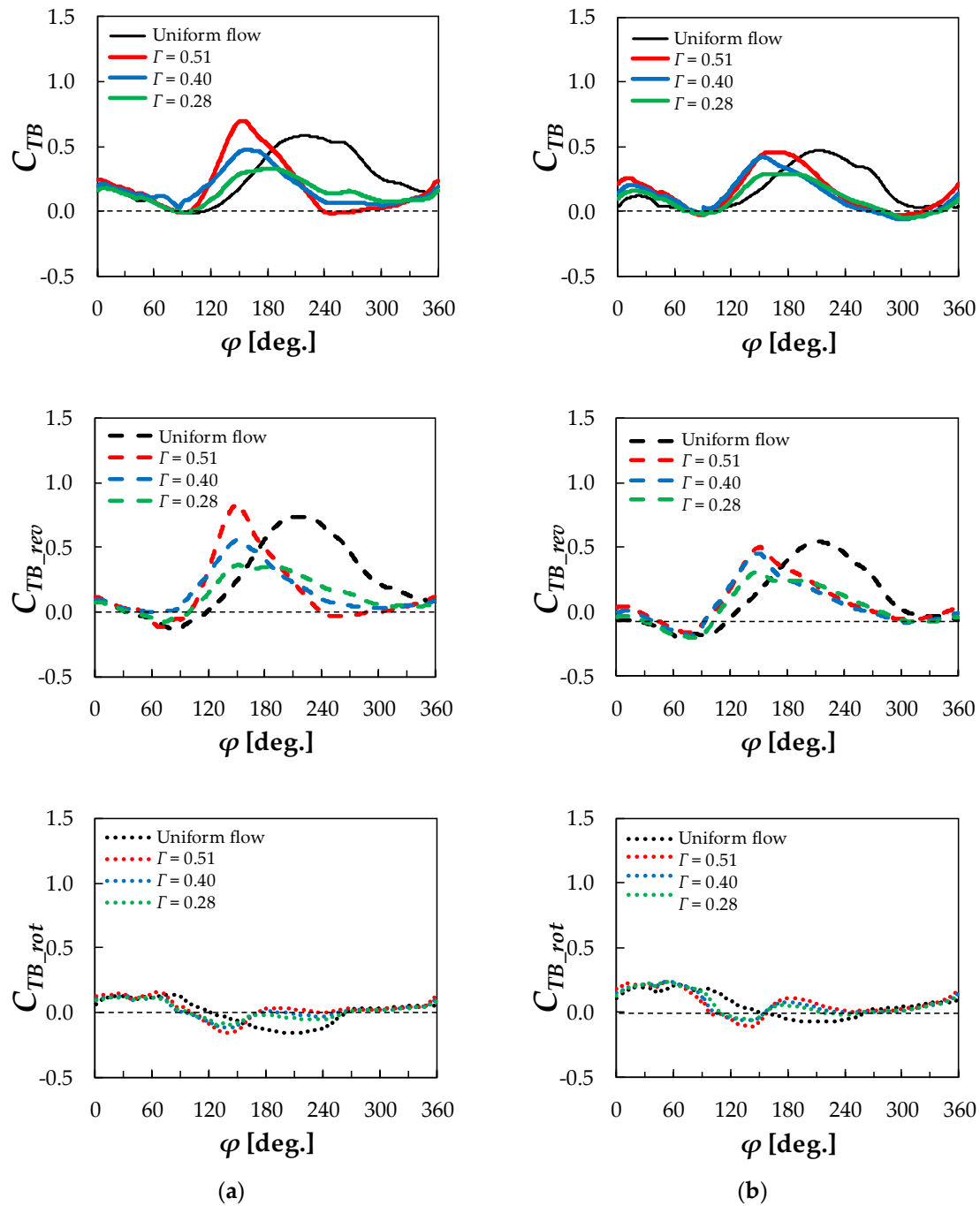


Figure 13. The variation of blade torque coefficient (C_{TB}), its rotor-revolution component (C_{TB_rev}) and its blade-rotation component (C_{TB_rot}) in the cases of the RSF-SF computed by the CFD simulations; (a) for $\lambda = 0.4$ and (b) for $\lambda = 0.6$. Noted that C_{TB} , C_{TB_rev} and C_{TB_rot} are coefficients of one blade.

4.3. Flow Characteristics

Figures 14a, 15a and 16a show the temporal sequence of the horizontal distributions of normalized horizontal velocity vectors, normalized pressure and normalized vorticity, respectively, at the mid-height of the O-VAWT at $\lambda = 0.4$ in the case of the uniform flow. At $\phi = 180^\circ$ to 270° , the approaching flow to the blade has a large velocity component perpendicular to the blade, and the pressure on the upwind side of the blade is high. Due to this high pressure, C_{TB_rev} is significantly high in the range of $\phi = 180^\circ$ to 270° in Figure 9. In addition, at $\phi = 210^\circ$ to 270° , due to the strong large vortex formed near the outer edge of the downwind side of the blade, the pressure is low near the

vortex. This low pressure positively contributes to C_{TB_rev} (see Figure 9 at $\varphi = 210^\circ$ to 270°). By contrast, this low pressure negatively contributes to C_{TB_rot} (see Figure 9 at $\varphi = 210^\circ$ to 270°). At $\varphi = 300^\circ$ and 330° , the approaching flow to the blade has a small velocity component perpendicular to the blade and the pressure on the upwind side of the blade is not high. Therefore, C_{TB_rev} is lower as compared to the upwind region of the advancing side of the rotor (see Figure 9 at $\varphi = 180^\circ$ to 270°). At $\varphi = 0^\circ$ to 120° , the attack angle of the blade is positive (here, the counterclockwise direction is defined as positive) and the flow separates over the outer side of the blade. Therefore, on the upwind edge of the blade and on the inner side of the blade near its upwind edge, the pressure is relatively high. In contrast, on the outer side of the blade near its upwind edge, the pressure is relatively lower. This pressure distribution contributes negatively to C_{TB_rev} and positively to C_{TB_rot} .

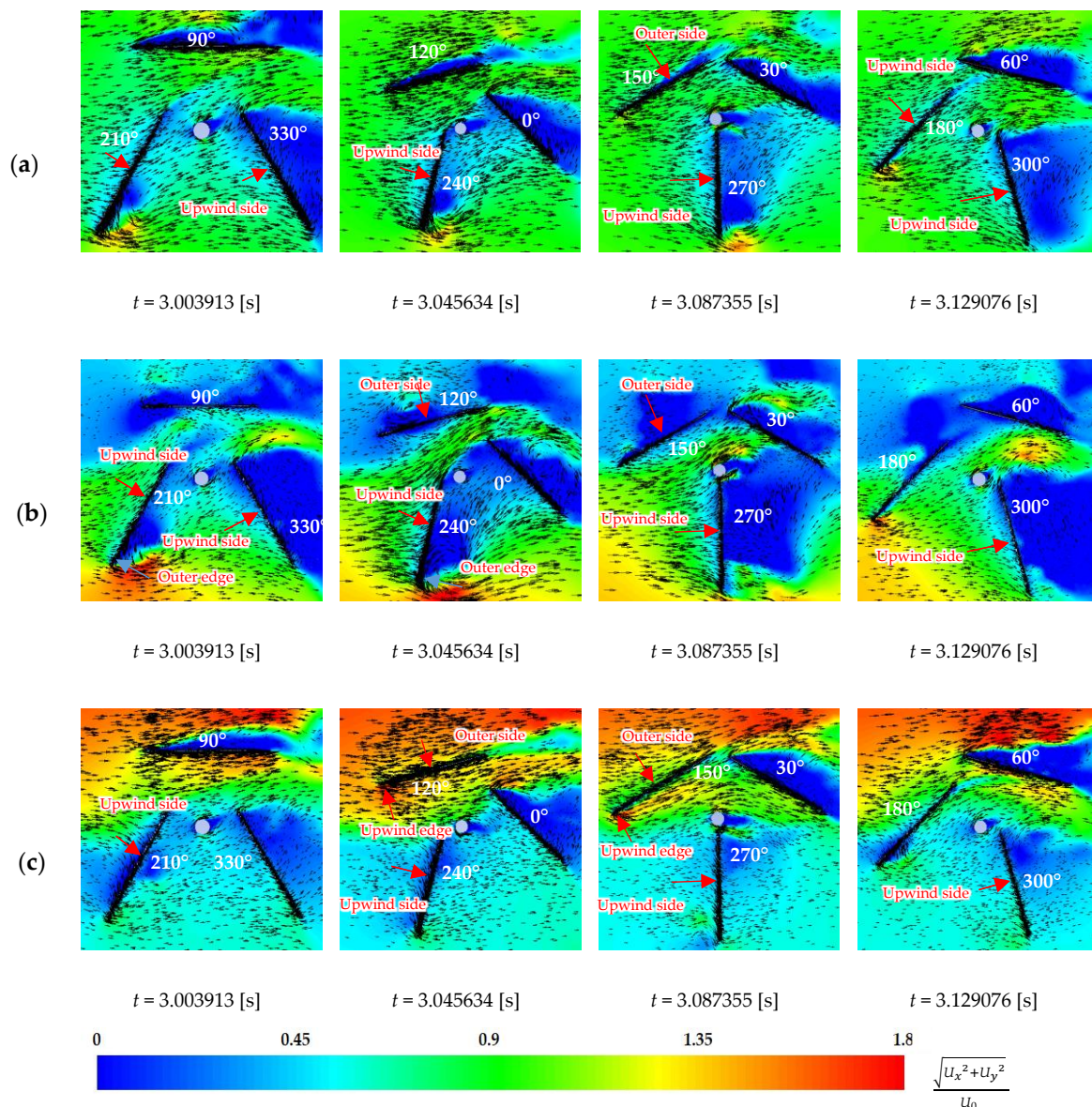


Figure 14. The temporal sequence of the horizontal distributions of normalized horizontal velocity vectors of the O-VAWT for $\lambda = 0.4$ in the case of; (a) the uniform flow, (b) the ASF-SF with $\Gamma = 0.51$ and (c) the RSF-SF with $\Gamma = 0.51$.

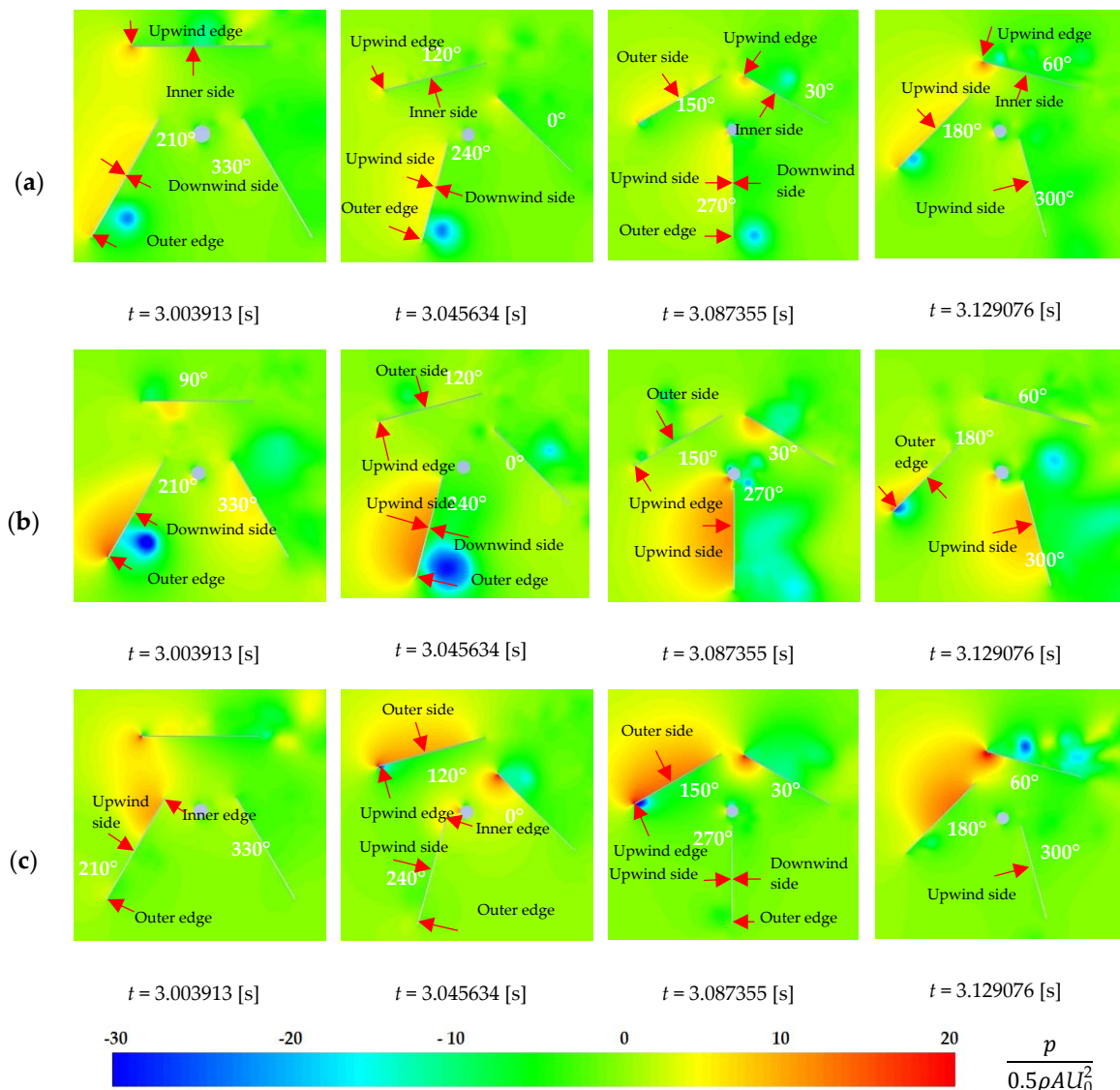


Figure 15. The temporal sequence of normalized pressure at the mid-height of the O-VAWT for $\lambda = 0.4$ in the case of; (a) the uniform flow, (b) the ASF-SF with $\Gamma = 0.51$ and (c) the RSF-SF with $\Gamma = 0.51$.

Figures 14b and 15b and Figure 16b show the temporal sequence of the horizontal distributions of normalized horizontal velocity vectors, normalized pressure and normalized vorticity, respectively, at the mid-height of the O-VAWT at $\lambda = 0.4$ in the case of the ASF-SF with $\Gamma = 0.51$. At $\varphi = 210^\circ$ to 330° , the approaching flow to the blade has a larger velocity component perpendicular to the blade, and the pressure on the upwind side of the blade is higher as compared to the uniform flow case. Due to this higher pressure, C_{TB_rev} is higher than the uniform flow case (see Figure 12 at $\varphi = 210^\circ$ to 330°). In addition, at $\varphi = 210^\circ$ to 240° , wind speed is significantly increased at the outer edge of the blade and a significantly stronger and larger vortex is formed near the outer edge on the downwind side of the blade. Near the vortex, the pressure is lower as compared to the uniform flow case. This low pressure contributes to higher C_{TB_rev} and lower C_{TB_rot} as compared to the uniform flow case (see Figure 12 at $\varphi = 210^\circ$ to 240°). At $\varphi = 120^\circ$ and 150° , the pressure on the outer side of the blade is lower due to the lower speed approaching flow to the blade. Furthermore, the pressure on the inner side of the blade near its upwind edge is higher due to the existence of the blade at $\varphi = 240^\circ$ or 270° , respectively. This pressure distribution contributes to lower C_{TB_rev} and higher C_{TB_rot} as compared to the uniform flow case (see Figure 12 at $\varphi = 120^\circ$ to 150°).

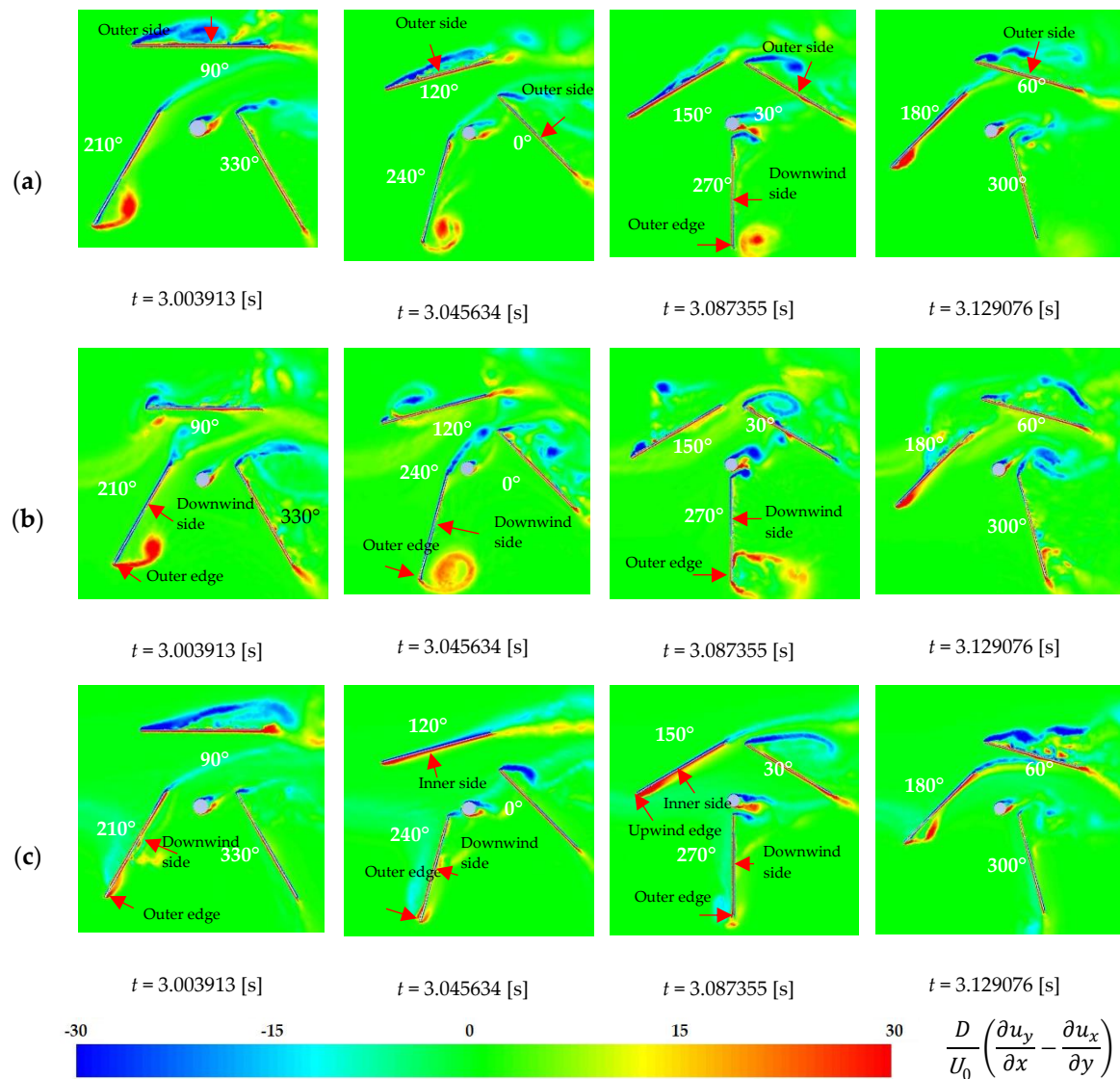


Figure 16. The temporal sequence of normalized vorticity at the mid-height of the O-VAWT for $\lambda = 0.4$ in the case of; (a) the uniform flow, (b) the ASF-SF with $\Gamma = 0.51$ and (c) the RSF-SF with $\Gamma = 0.51$.

Figures 14c, 15c and 16c show the temporal sequence of normalized horizontal distributions of horizontal velocity vectors, pressure and vorticity, respectively, at the mid-height of the O-VAWT at $\lambda = 0.4$ in the case of the RSF-SF with $\Gamma = 0.51$. At $\varphi = 120^\circ$ and 150° , the approaching flow to the blade has a larger velocity component perpendicular to the blade and the pressure on the outer side of the blade is higher as compared to the uniform flow case. Due to this higher pressure, C_{TB_rev} is higher than the uniform flow case (see Figure 13 at $\varphi = 120^\circ$ and 150°). Furthermore, wind speed is increased at the upwind edge of the blade and a stronger vortex is formed near the upwind edge of the blade on its inner side. Near the vortex, the pressure is lower as compared to the uniform flow case. This low pressure contributes to higher C_{TB_rev} and lower C_{TB_rot} as compared to the uniform flow case (see Figure 13 at $\varphi = 120^\circ$ and 150°). At $\varphi = 210^\circ$ to 300° , except in the vicinity of the upwind side of the inner edge of the blade at $\varphi = 210^\circ$, the approaching flow to the blade has a smaller velocity component perpendicular to the blade and the pressure on the upwind side of the blade is lower as compared to the uniform flow case. Due to this lower pressure, C_{TB_rev} is lower than the uniform flow case (see Figure 13 at $\varphi = 210^\circ$ and 300°). In addition, at $\varphi = 210^\circ$ and 240° , the vortex formed near the outer edge of the downwind side of the blade is weaker and the pressure drop becomes smaller as

compared to the uniform flow case. This smaller pressure drop contributes to lower C_{TB_rev} and higher C_{TB_rot} as compared to the uniform flow (see Figure 13 at $\varphi = 210^\circ$ and 240°).

5. Conclusions

We investigated the effects of horizontal shear flow on the performance characteristics of an orthopter-type vertical axis wind turbine (O-VAWT) by conducting wind tunnel experiments and computational fluid dynamics (CFD) simulations. In addition to a uniform flow, two types of shear flow were used as the approaching flow to the O-VAWT. One type was an advancing side faster shear flow (ASF-SF), which had a higher velocity on the advancing side of the rotor. The other type was a retreating side faster shear flow (RSF-SF), which had a higher velocity on the retreating side of the rotor. For each type of shear flow, we set three different velocity ratios ($\Gamma = 0.28, 0.40$ and 0.51), which were the ratios of the difference between the highest velocity and the lowest velocity in a shear flow to the sum of the highest and lowest velocities. The main findings are summarized as follows:

1. In the ASF-SF cases, the power coefficients (C_p) were significantly higher than the uniform flow case at all tip speed ratios (λ) and increased with Γ . The experimental results for the maximum C_p of the ASF-SF case with $\Gamma = 0.51$ and the uniform flow case were 0.43 when $\lambda = 0.6$ and 0.32 when $\lambda = 0.4$, respectively. Around the optimal λ , the blade torque coefficient (C_{TB}) on the advancing side of the rotor was, in general, significantly higher than the uniform flow case and increased with Γ , predominantly contributing to the increase in C_p . The CFD results for the maximum discrepancies of C_{TB} on the advancing side of the rotor between the ASF-SF case with $\Gamma = 0.51$ and the uniform flow case were 0.38 when $\lambda = 0.4$ and 0.44 when $\lambda = 0.6$. The high values of C_{TB} of the ASF-SF cases on the advancing side of the rotor were mainly caused by the higher pressure on the upwind side of the blade due to the higher speed of the approaching flow and by the lower pressure near the outer edge of the downwind side of the blade due to the formation of a larger vortex.
2. In the RSF-SF cases, C_p increased with Γ . However, when $\Gamma = 0.28$, C_p was lower than the uniform flow case at all λ . When $\Gamma = 0.51$, C_p was higher than the uniform flow case except at low λ ; however, it was lower than the ASF-SF case with $\Gamma = 0.28$. The experimental results for the maximum C_p of the RSF-SF case with $\Gamma = 0.28$, the RSF-SF case with $\Gamma = 0.51$ and the ASF-SF case with $\Gamma = 0.28$ were 0.29 when $\lambda = 0.4$, 0.33 when $\lambda = 0.5$ and 0.35 when $\lambda = 0.5$, respectively. Around the optimal λ , the blade torque coefficient (C_{TB}) on the retreating side of the rotor was, in general, higher than the uniform flow case and increased with Γ , predominantly contributing to the increase in C_p . The CFD results for the maximum discrepancies of C_{TB} on the retreating side of the rotor between the RSF-SF case with $\Gamma = 0.51$ and the uniform flow case were 0.60 when $\lambda = 0.4$ and 0.36 when $\lambda = 0.6$. The high values of C_{TB} of the RSF-SF cases on the retreating side of the rotor were mainly caused by the higher pressure on the outer side of the blade on the upwind side of the rotor, due to the higher speed of the approaching flow. By contrast, C_{TB} on the advancing side of the rotor was, in general, lower than the uniform flow case, due to the lower pressure on the upwind side of the blade.
3. C_{TB} consists of the rotor-revolution component (C_{TB_rev}) and the blade-rotation component (C_{TB_rot}). In all the shear flow cases, as well as the uniform flow case, the contributions of C_{TB_rev} to C_{TB} were dominant. The dependencies of C_{TB_rev} and C_{TB_rot} on Γ had the opposite tendencies.

These findings are useful for micro-siting of an O-VAWT in the area where shear flows occur. A location where ASF-SFs with high Γ values dominantly occur is ideal for installing the O-VAWT. At a location where not only ASF-SFs but also RSF-SFs occur at high frequencies, higher Γ values are preferable. However, the shear flows utilized in this study are limited in their profiles and the relative positions to the rotor. To properly conduct the micro-siting of an O-VAWT in the area where various kinds of shear flows occur, such as the vicinity of a building, it is essential to understand the performance characteristics of the O-VAWT in the various kinds of shear flows. Therefore, in future research, we plan to investigate the effects of the broadness of the shear layer and the relative position

of the shear flow to the rotor on the O-VAWT's performance characteristics. In addition, we plan to investigate the effects of the turbulence intensity of the approaching flow on the CFD results for the O-VAWT's performance characteristics by setting obstacles, which emit eddies, upwind of the O-VAWT to avoid the rapid dissipation of high turbulence intensity.

Author Contributions: R.P.W. performed the numerical simulations and prepared this manuscript being supervised by T.K. (Takaaki Kono). All authors contributed to the analyses of the data. T.K. (Takaaki Kono) and T.K. (Takahiro Kiwata) supervised the entire work. All authors have read and agreed to the published version of the manuscript.

Funding: This research was funded by World Bank Loan No. 8245-ID and a grant from Takahashi Industrial and Economic Research Foundation.

Acknowledgments: This research was supported by the Program for Research and Innovation in Science and Technology (RISET-Pro) Kemenristekdikti. The authors are thankful to technician Kuratani and student Taiki Sugawara for their help with the experiment.

Conflicts of Interest: The authors declare no conflict of interest.

References

1. Bahaj, A.S.; Myers, L.; James, P.A.B. Urban energy generation: Influence of micro-wind turbine output on electricity consumption in buildings. *Energy Build.* **2007**, *39*, 154–165. [[CrossRef](#)]
2. Toja-Silva, F.; Colmenar-Santos, A.; Castro-Gil, M. Urban wind energy exploitation systems: Behaviour under multidirectional flow conditions—Opportunities and challenges. *Renew. Sustain. Energy Rev.* **2013**, *24*, 364–378. [[CrossRef](#)]
3. Ishugah, T.F.; Li, Y.; Wang, R.Z.; Kiplagat, J.K. Advances in wind energy resource exploitation in urban environment: A review. *Renew. Sustain. Energy Rev.* **2014**, *37*, 613–626. [[CrossRef](#)]
4. Tummala, A.; Velamati, R.K.; Sinha, D.K.; Indraja, V.; Krishna, V.H. A review on small scale wind turbines. *Renew. Sustain. Energy Rev.* **2016**, *56*, 1351–1371. [[CrossRef](#)]
5. Kumar, R.; Raahemifar, K.; Fung, A.S. A critical review of vertical axis wind turbines for urban applications. *Renew. Sustain. Energy Rev.* **2018**, *89*, 281–291. [[CrossRef](#)]
6. Stathopoulos, T.; Alrawashdeh, H.; Al-Quraan, A.; Blocken, B.; Dilimulati, A.; Paraschivoiu, M.; Pilay, P. Urban wind energy: Some views on potential and challenges. *J. Wind Eng. Ind. Aerodyn.* **2018**, *179*, 146–157. [[CrossRef](#)]
7. Toja-Silva, F.; Kono, T.; Peralta, C.; Lopez-Garcia, O.; Chen, J. A review of computational fluid dynamics (CFD) simulations of the wind flow around buildings for urban wind energy exploitation. *J. Wind Eng. Ind. Aerodyn.* **2018**, *180*, 66–87. [[CrossRef](#)]
8. Anup, K.C.; Whale, J.; Urmee, T. Urban wind conditions and small wind turbines in the built environment: A review. *Renew. Energy* **2019**, *131*, 268–283.
9. Carbó Molina, A.; De Troyer, T.; Massai, T.; Vergaerde, A.; Runacres, M.C.; Bartoli, G. Effect of turbulence on the performance of VAWTs: An experimental study in two different wind tunnels. *J. Wind Eng. Ind. Aerodyn.* **2019**, *193*, 103969. [[CrossRef](#)]
10. Wood, D. *Small Wind Turbines*; Green Energy and Technology; Springer: London, UK, 2011; ISBN 978-1-84996-174-5.
11. Manwell, J.F.; McGowan, J.G.; Rogers, A.L. *Wind Energy Explained: Theory, Design and Application*; John Wiley & Sons: Hoboken, NJ, USA, 2010; ISBN 9780470015001.
12. Allen, S.R.; Hammond, G.P.; McManus, M.C. Prospects for and barriers to domestic micro-generation: A United Kingdom perspective. *Appl. Energy* **2008**, *85*, 528–544. [[CrossRef](#)]
13. Islam, M.; Ting, D.S.K.; Fartaj, A. Aerodynamic models for Darrieus-type straight-bladed vertical axis wind turbines. *Renew. Sustain. Energy Rev.* **2008**, *12*, 1087–1109. [[CrossRef](#)]
14. Jin, X.; Zhao, G.; Gao, K.; Ju, W. Darrieus vertical axis wind turbine: Basic research methods. *Renew. Sustain. Energy Rev.* **2015**, *42*, 212–225. [[CrossRef](#)]
15. Ghasemian, M.; Ashrafi, Z.N.; Sedaghat, A. A review on computational fluid dynamic simulation techniques for Darrieus vertical axis wind turbines. *Energy Convers. Manag.* **2017**, *149*, 87–100. [[CrossRef](#)]
16. Kumar, P.M.; Sivalingam, K.; Narasimalu, S.; Lim, T.-C.; Ramakrishna, S.; Wei, H. A review on the evolution of darrieus vertical axis wind turbine: Small wind turbines. *J. Power Energy Eng.* **2019**, *7*, 27–44. [[CrossRef](#)]

17. Abraham, J.P.; Plourde, B.D.; Mowry, G.S.; Minkowycz, W.J.; Sparrow, E.M. Summary of Savonius wind turbine development and future applications for small-scale power generation. *J. Renew. Sustain. Energy* **2012**, *4*, 042703. [[CrossRef](#)]
18. Akwa, J.V.; Vielmo, H.A.; Petry, A.P. A review on the performance of Savonius wind turbines. *Renew. Sustain. Energy Rev.* **2012**, *16*, 3054–3064. [[CrossRef](#)]
19. Roy, S.; Saha, U.K. Review on the numerical investigations into the design and development of Savonius wind rotors. *Renew. Sustain. Energy Rev.* **2013**, *24*, 73–83. [[CrossRef](#)]
20. Kang, C.; Liu, H.; Yang, X. Review of fluid dynamics aspects of Savonius-rotor-based vertical-axis wind rotors. *Renew. Sustain. Energy Rev.* **2014**, *33*, 499–508. [[CrossRef](#)]
21. Alom, N.; Saha, U.K. Evolution and progress in the development of savonius wind turbine rotor blade profiles and shapes. *J. Sol. Energy Eng. Trans. ASME* **2019**, *141*, 1–15. [[CrossRef](#)]
22. Elkhoury, M.; Kiwata, T.; Nagao, K.; Kono, T.; ElHajj, F. Wind tunnel experiments and Delayed Detached Eddy Simulation of a three-bladed micro vertical axis wind turbine. *Renew. Energy* **2018**, *129*, 63–74. [[CrossRef](#)]
23. Kiwata, T. Vertical axis wind turbine with variable-pitch straight blades. In Proceedings of the International Conference on Jets, Wakes and Separated Flows, ICJWSF-2017, Cincinnati, OH, USA, 9–12 October 2017; pp. 1–6.
24. Shimizu, Y.; Maeda, T.; Kamada, Y.; Takada, M.; Katayama, T. Development of micro wind turbine (Orthoptere Wind Turbine). In Proceedings of the International Conference on Fluid Engineering JSME Centennial Grand Congress, Tokyo, Japan, 13–16 July 1997; pp. 1551–1556.
25. Bayeul-Laine, A.-C.; Simonet, S.; Dockter, A.; Bois, G. Numerical study of flow stream in a mini VAWT with relative rotating blades. In Proceedings of the 22nd International Symposium on Transport Phenomena Conference, Delft, The Netherlands, 8–11 November 2011; p. 13.
26. Cooper, P.; Kennedy, O.C.; Cooper, P.; Kennedy, O. Development and analysis of a novel vertical axis wind turbine development and analysis of a novel vertical axis wind turbine. In Proceedings of the Solar 2004: Life, The Universe and Renewables, Perth, Australia, 30 November–3 December 2004; pp. 1–9.
27. Kono, T.; Kogaki, T.; Kiwata, T. Numerical investigation of wind conditions for roof-mounted wind turbines: Effects of wind direction and horizontal aspect ratio of a high-rise cuboid building. *Energies* **2016**, *9*, 907. [[CrossRef](#)]
28. Balduzzi, F.; Bianchini, A.; Ferrari, L. Microeolic turbines in the built environment: Influence of the installation site on the potential energy yield. *Renew. Energy* **2012**, *45*, 163–174. [[CrossRef](#)]
29. Ferreira, C.J.S.; Van Bussel, G.J.W.; Van Kuik, G.A.M. Wind tunnel hotwire measurements, flow visualization and thrust measurement of a VAWT in skew. *J. Sol. Energy Eng. Trans. ASME* **2006**, *128*, 487–497. [[CrossRef](#)]
30. Burton, T.; Jenkins, N.; Sharpe, D.; Bossanyi, E. *Wind Energy Handbook*, 2nd ed.; John Wiley & Sons: Hoboken, NJ, USA, 2011; ISBN 9780470699751.
31. ANSYS, Inc. *ANSYS Fluent Theory Guide, Release 17.2*; ANSYS, Inc.: Canonsburg, PA, USA, 2016.
32. ANSYS, Inc. *ANSYS Fluent User Guide, Release 17.2*; ANSYS, Inc.: Canonsburg, PA, USA, 2016.
33. ElCheikh, A.; Elkhoury, M.; Kiwata, T.; Kono, T. Performance analysis of a small-scale orthoptere-type vertical axis wind turbine. *J. Wind Eng. Ind. Aerodyn.* **2018**, *180*, 19–33. [[CrossRef](#)]
34. Spalart, P.R.; Jou, W.H.; Strelets, M.; Allmaras, S.R. Comments on the feasibility of LES for wings, and on a hybrid RANS/LES approach. In Proceedings of the First AFOSR International Conference on DNS/LES, Ruston, LA, USA, 4–8 August 1997; pp. 137–147.
35. Tominaga, Y.; Mochida, A.; Yoshie, R.; Kataoka, H.; Nozu, T.; Yoshikawa, M.; Shirasawa, T. AIJ guidelines for practical applications of CFD to pedestrian wind environment around buildings. *J. Wind Eng. Ind. Aerodyn.* **2008**, *96*, 1749–1761. [[CrossRef](#)]
36. Wu, H.; Stathopoulos, T. Wind-tunnel techniques for assessment of pedestrian-level winds. *J. Eng. Mech.* **1993**, *119*, 1920–1936. [[CrossRef](#)]
37. Tian, W.; Mao, Z.; Zhang, B.; Li, Y. Shape optimization of a Savonius wind rotor with different convex and concave sides. *Renew. Energy* **2018**, *117*, 287–299. [[CrossRef](#)]

